J. COMBIN. MATH. COMBIN. COMPUT. 127a (2025) 5533--5555

Journal of Combinatorial Mathematics and Combinatorial Computing
www.combinatorialpress.com/jcmcc

Combinatorial Press

Research on the analysis of bridge quality monitoring data based on laser point cloud technology

Xiaoqiang Tang[1,✉], Kai Wang[1], Chengbo Lu[2]

[1] *PowerChina Road & Bridge Group Co., Ltd., Beijing, 100160, China*

[2] *Xinjiang Agricultural University, Urumuqi, Xinjiang, 830000, China*

ABSTRACT

Bridge construction is an important link in the construction of transportation infrastructure, which plays a key role in ensuring the smoothness and safety of road traffic. This paper systematically organizes the process of laser point cloud technology in bridge quality monitoring, and proposes an improved adaptive hyperparametric RANSAC point cloud segmentation algorithm to realize the bridge quality monitoring. Firstly, the basic process of RANSAC algorithm is sorted out, and the mean downsampling operation is adopted to replace the center of gravity downsampling method, which improves the point average degree of downsampling. Next, the FPS algorithm is combined with the method of selecting seed points to expand the range of selected values of seed points under the premise of meeting the relevant requirements. After splitting multiple fitting surfaces, the split fitting surfaces are combined to optimize the unfitted points and improve the fitting rate of the algorithm. The detection accuracy of the bearing flatness of bridge number 3 under the method of this paper is improved by 78.26%, and the maximum deviation of the detected bridge constitutive point offset is only 0.623m, which is within the acceptable range of bridge error monitoring. The feasibility of laser point cloud technology for bridge quality monitoring is verified.

Keywords: Point cloud segmentation, RANSAC; FPS algorithm, bridge quality monitoring, laser point cloud technology

1. Introduction

Transportation has always played a key role in the national economy, and the two are inseparable, promoting each other and developing together [1-2]. Nowadays, China is the country with the largest number of bridges in the world, and with the increasing mileage of highway operation, the number of bridges with existing operation, maintenance and repair is gradually expanding, which is not only related to the economic lifeline of the nation, but also tightly connected to the life of the nation [3-6].

✉ Corresponding author.
E-mail address: tangxiaoqiang6@163.com (X. Tang).
Received 20 March 2024; Revised 05 June 2024; Accepted 20 November 2024; Published Online 15 April 2025.
DOI: 10.61091/jcmcc127a-309

As an important part of the highway, the regular monitoring and maintenance of bridge health has become increasingly severe under the joint influence of the growing traffic squeeze and the ground hazard caused by extreme weather [7-10]. In addition, with the significant advances in computer science, construction technology, and structural mechanics, many bridges with special structures that were previously difficult to manufacture have begun to appear gradually [11-13]. Therefore, there is an urgent need to find a highly accurate, efficient and intelligent way to deal with bridge safety.

Early bridge inspection methods are time-consuming and costly in terms of labor, low inspection accuracy, and although there are fixed standards, there are still artificial influencing factors, such as the inspector's experience and mental concentration, which will bring uncertainty to the inspection results [14-17]. With the continuous development of laser technology, laser point cloud measurement has become the mainstream technology of current mapping technology [18]. A variety of laser measurement means, such as airborne laser, vehicle-mounted laser, ground laser, backpack laser, etc., satisfy the acquisition needs of different business models and different measurement scenarios, and this acquisition means has high efficiency, high accuracy, and reliable data quality [19-22]. Vehicle-mounted laser acquires the laser point cloud of the road pavement range and ground laser acquires the laser point cloud of the upper and lower structure of the bridge, and the point cloud data of the whole bridge can be obtained through the alignment of the point cloud, so as to realize the reverse model flipping, which makes it feasible to monitor the three-dimensional visualization of the bridge for a long time operation bridge [23-26]. Therefore, it has become a new effective method to obtain the laser point cloud data of bridges for modeling and analysis through different laser acquisition methods.

Bridge quality inspection method is based on non-destructive testing method, and non-destructive testing method can be divided into elastic wave radar detection method, surface wave detection method, ultrasonic detection method, image processing detection method and so on. The elastic wave radar detection method is mainly through the reception of the corresponding signal reflected back and extracted, and then processed by image processing. Maizuar, M. et al. designed a bridge condition assessment framework with integrated computational modeling and non-contact radar sensors (IBIS-S) to measure frequency variations in the vibration response of bridges for quality monitoring [27]. Zhang, G. et al. showed that bridge stiffness can reflect the load carrying capacity of a bridge, and proposed microwave interference radar technique and curvature envelope area identification method, which can be used to identify the stiffness of a bridge distribution unit in two scenarios, undamaged or damaged [28]. Yaghoubzadehfard, A. et al. introduced an interferometric radar system for imaging bridge structures through interferometric frequencies, which, in combination with machine learning techniques, can be used to further analyze the modal parameters of bridges in order to accomplish structural health monitoring of bridges [29]. Mizutani, T. et al. proposed a non-contact radar detection method based on UHF fast scanning for the assessment of the structural conditions of bridge panels, and by analyzing the reflected wave signals, it is possible to construct a visual model of a full-size bridge panel [30]. The advantages of the elastic wave radar detection method are high detection accuracy and the ability to identify defects within the structure without direct contact, the disadvantage is that the equipment is too large and heavy, not easy to carry and use artificially, in addition to the need to match the use of heavy construction machinery.

The principle of surface wave detection is based on the relationship between the depth and the rebound strength of the wave to determine the depth of cracks. Baba, S. et al. proposed a bridge quality monitoring method based on acoustic surface wave sensors, which is a mass-produced and inexpensive identification system for structural health monitoring of bridge projects [31]. Mahvelati, S. et al. discussed the feasibility of multi-channel surface wave technology for assessing bridge engineering structures, which demonstrated good accuracy in the assessment of transverse dimensions of embedded foundations [32]. Xiao, H. et al. designed a novel non-destructive standing wave bridge inspection system and algorithm, which analyzes the standing waves formed between the equipment and the inspected bridge, and provides a detailed understanding of the inspected object's health state and has high detection sensitivity and accuracy [33]. Heymann, G. et al. outlined the superiority of continuous surface wave ground stiffness testing and nonlinear elastic settlement analysis of bridge structures, pointing out that the stiffness data obtained by the proposed method in bridge simulated load experiments can accurately reflect the settlement problem of bridges [34]. It can be found that the surface wave inspection method is very effective for defect detection near the surface, and the accuracy can reach the millimeter level, but its use is more complicated and highly specialized.

Ultrasonic inspection method is also for the detection of internal defects of bridge body. Nguyen, T. D. et al. used the full waveform inversion technique to invert the ultrasonic surface wave field in bridge detection, and their analytical results are valid in detecting the delamination of concrete decks[35]. Chakraborty, J. et al. developed an embedded monitoring system for bridge durability assessment which based on the results of ultrasonic transducer response analysis can effectively detect abnormal conditions of structural properties of bridges [36]. Sanderson, T. et al. investigated the non-destructive testing technique of bridge panels by deploying the ultrasonic tomography equipment, MIRA, on bridge panels, which can evaluate the internal structure of bridge panels by ultrasonic scanning [37]. Erdogmus, E. et al. examined ultrasonic inspection methods for reinforced concrete bridge deck inspection, discussed ultrasonic transmission limitations inside concrete, etc., and gave relevant optimization recommendations [38]. Although the ultrasonic inspection method is highly accurate, it is more susceptible to interference from other factors, such as humidity and material, than elastic waves, and requires a strong degree of specialization.

The image detection method is to intercept the image or video through the camera, which can be used to analyze the bridge body in real time or record the video, and can be combined with robots or drones to carry out automated inspection, which is more in line with the future development trend of intelligence. Therefore, the laser point cloud technology can be used to record the deformation data of the bridge body for a long time, and combined with the finite element analysis for a comprehensive analysis of the bridge body.

In this paper, the spatial information provided by laser electric cloud technology is used as a support to map the spatial information of the bridge building using 3D laser point cloud technology. The improved RANSAC algorithm is used to segment the bridge point cloud data. The downsampling process of the point cloud data is added to the hyperparametric RANSAC algorithm to reduce the number of seed points of the point cloud data. The downsampling replaces the feature points in the original grid, which improves the downsampling homogeneity of the point cloud data. In addition, the manual selection method of the height threshold of the hyperparametric RANSA fitting process was optimized to an adaptive selection method to obtain more accurate segmentation results. After obtaining the segmentation results, the fitted facets are merged to reduce the overfitting effect. Finally, the processing of unfitted points is optimized to reduce the unfitting rate of the algorithm. The algorithm of this paper is compared with the traditional monitoring algorithm, and then the algorithm is applied to the bridge monitoring example analysis to verify the monitoring accuracy of the algorithm of this paper.

2. Research on bridge quality inspection based on 3D laser scanning technology

2.1. Composition and working principle of 3D laser scanning system

Three-dimensional laser scanning system [39] has many accessories together, including the target, scanner, color CCD camera, etc., which is a kind of transmission equipment through the scanning rotation to the object to be measured to do a comprehensive measurement of the operation, and by the internal processing of the instrument, so as to obtain the scanning of the surface of the object of the massive cloud of point information.

Three-dimensional laser scanner point cloud data collected by the laser beam of the horizontal and vertical direction value, the scanning point of the space relative three-dimensional coordinates, the point cloud of the reflective intensity of the three parts of the data acquisition process applied to the principle of light reflection. The 3D laser scanner receives the reflection angle of the laser signal on the target to be measured and stores it as the horizontal and vertical values, and then combines it with the distance between the target to be measured and the scanner to get the relative 3D coordinates of the scanning point in space. Three-dimensional laser scanning system to the instrument's own coordinate system as a benchmark, in general, different devices on the definition of the coordinates are different. Conventionally, the coordinate origin is expressed as the laser beam emission point, the Z-axis points to the big sky, and the Y-axis is along the direction of the water-half laser beam, in which the X, Y and Z axes are in accordance with the right-handed criterion, and the formulas for calculating the scanning point in the system are as follows:

$$Xp = S\cos\theta\cos\partial \tag{1}$$

$$Yp = S\cos\theta\sin\partial \tag{2}$$

$$Zp = S\sin\theta \tag{3}$$

Laser ranging is the main part of this scanner, in which the methods are: phase, pulse, triangulation and pulse-phase methods when performing ranging.

Pulse ranging method [40] is based on the principle that the laser signal emitted by the laser reflector is diffusely reflected when it reaches the target to be measured, and the laser signal is received by the receiver, and the signal round trip time is recorded. The distance between the instrument and the target to be measured can be calculated using the formula, and finally converted into data information that can be directly recognized and processed, and output through software processing.

$$2D = \frac{C_0}{n_r} t_D \tag{4}$$

Where C_0 is the vacuum speed of light value, general curve 299792458m/s; n_r is the atmospheric refractive index.

Modulation of light round-trip 1 times the appearance of the phase delay, followed by the combination of its signal wavelength, the spacing of the phase delay is converted, you can calculate the light through the round-trip line of measurement time t. This topic uses the Z + F5010x three-dimensional laser scanner that utilizes the principle of phase-type ranging, to obtain the point cloud data information. This three-dimensional laser scanner measurement distance is small, generally within 100m, point sampling rate of up to 10K ~ 50K points per second, point cloud accuracy, generally millimeter-level, fast scanning speed.

$$L = \frac{1}{2}ct \tag{5}$$

$$t = \frac{\varphi}{\varpi} = \frac{2\pi N + \Delta\varphi}{2\pi f} = (N + \frac{\Delta\varphi}{2\pi})\frac{1}{f} \tag{6}$$

Substituting equation (5) into equation (6) gives:

$$L = \frac{1}{2}ct = \frac{c}{2}(N + \frac{\Delta\varphi}{2\pi})\frac{1}{f} = \frac{\lambda}{2}(N + \frac{\Delta\varphi}{2\pi}) \tag{7}$$

Triangulation is a combination of triangular geometric relationships to calculate the distance from the center of the scanner to the target, including the CCD lens, the reflection point of the object to be measured and the laser transmitter three parts. The laser is emitted to the surface of the object to be measured to get the angle between the incident beam and the reflected beam, and get the distance change generated by the change in position, through the triangular geometric relationship between the scanner and the object to deduce the distance. Triangulation not only has the characteristics of real-time, but also has good accuracy, currently, this method is commonly used in agriculture, industry and military and other fields.

2.2. Classification and Applications of 3D Laser Scanning Systems

Three-dimensional laser scanners can be categorized into various types based on the carrier used, namely, portable three-dimensional laser scanners, terrestrial three-dimensional scanners, vehicle-mounted and airborne three-dimensional laser scanners. Airborne 3D laser scanners are widely used for drawing mobile maps, conducting disaster monitoring and environmental monitoring, and agricultural and forestry protection. Their main features are; the ability to provide dense point cloud data, the ability to penetrate dense vegetation, contactless or less contact measurement, and the ability to measure both ground and non-ground layers. The vehicle-mounted 3D laser scanner system, on the other hand, integrates the scanner in a mobile vehicle, and is mainly used in in digital cities, urban roads, rail transportation, etc. Ground three-dimensional scanner through the operation of the ground computer digging system, transmitting light signals, collect the data information to be area, ground three-dimensional laser scanner compared to the first two cost-effective, handy eye fast, widely used in the mine survey most and deformation monitoring and so on. Portable three-dimensional laser scanner has more advantages, such as very lightweight, easy to carry, currently in the medical orthopedics, automobile manufacturing, industrial design and other fields are widely used.

According to the scanning distance range of the laser scanner, the laser scanner can be divided into three kinds of scanning systems: near distance, medium distance and long distance.

For the target object to be measured, the detection of it using 3D laser scanner mainly contains two important parts, i.e., the acquisition of point cloud data and the processing of data in the industry. Among them, a full-range, contactless scanning of the target using the 3D laser scanner is carried out to obtain solid point cloud spatial information, while the post-processing of the in-industry data must be operated through several steps of data manipulation, such as point cloud streamlining, denoising, and alignment, so as to establish a digital point cloud model of the target to be measured.

Data pre-processing refers to the use of 3D laser scanner manufacturers to provide supporting software to deal with point cloud data. Data processing mainly includes data noise reduction, alignment and compression. The purpose of data compression is to minimize the amount of data under the condition of ensuring the integrity of the point cloud data, so as to improve the data processing speed. The purpose of data alignment is to use the built-in algorithm to stitch together the point clouds scanned by different stations, so that the point cloud data obtained by different observation stations are in the same spatial coordinate system. The purpose of data noise reduction is to remove the useless noise points in the collected point cloud data, and finally get the streamlined, complete and accurate 3D point cloud model, the application flow chart of the model is shown in Figure 1.

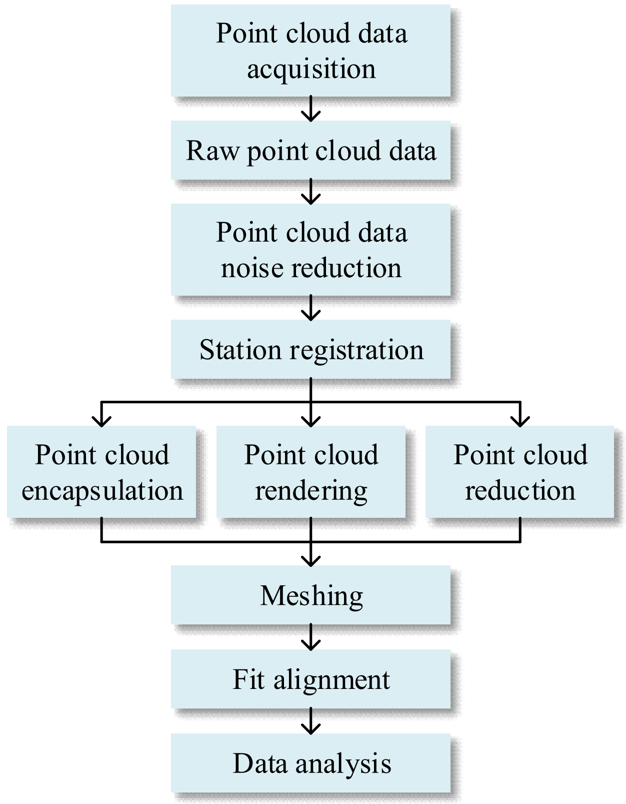

Fig. 1. Application flow chart

3. Based on improved RANSAC point cloud segmentation algorithm

3.1. Point cloud alignment process

Point cloud alignment is a spatial transformation of two or more groups of point clouds in different coordinate systems to the same coordinate system. The alignment process consists of two basic steps:
1) Establish the correspondence between the two sets of point clouds.
2) Solve the spatial transformation between the two sets of point clouds.

The above two steps can be achieved by minimizing a specific distance function, and after the first step is completed the optimal solution is computed, which ultimately makes the point cloud accurately aligned, and the next step is to define the point cloud alignment problem by means of mathematical modeling. Given two sets of point clouds in R^m space, representing shape point clouds and model point clouds, where m is the spatial dimension of the point clouds (this paper focuses on the alignment problem of 3D point clouds, in addition to the alignment of 2D point clouds), assuming that there exists some kind of mapping relationship $C:S \to M$ with the spatial transformations T from point cloud S to point cloud M, there exists a similarity metric model:

$$J(T(S), C(S)) \tag{8}$$

The alignment process of the point cloud can be reduced to the following optimization problem:

$$\min_{C,T} J(T(S), C(S)) \tag{9}$$

In the process of minimizing the distance function J, the correspondence C of two point clouds is established firstly, and then the optimal solution of the spatial transformation T is computed. In this optimization problem, the C and T of the two sets of point clouds must be solved at the same time, and this step is the focus and difficulty of the point cloud alignment process. The choice of J greatly affects the result of the alignment. Currently, the commonly used distance functions J are

Euclidean distance, Mahalanobs distance, Hausdorff [41] distance and so on.

In order to complete the rigid-body alignment of the point cloud, it is necessary to choose a suitable method to calculate the spatial transformation between the two point clouds T. According to the type of "deformation" that occurs between the two point clouds, it is divided into two types of alignment categories, i.e., the rigid-body alignment of the point cloud and the non-rigid-body alignment of the point cloud. The rigid-body alignment of point cloud is that the distance between the two point clouds to be aligned does not change in the process of moving, so the rigid-body alignment of point cloud mainly solves the spatial rotation variable R and translation variable t; the non-rigid-body alignment of point cloud is not the same as the rigid-body alignment, and in the process of the actual acquisition of data, the image is often deformed, so it involves the non-rigid-body transformations, such as the similarity transformations, the expansion transformations, the affine transformation, the projection transformations and the elasticity transformations, etc. The projective transformations and the elasticity transformations, etc., are the same as the rigid-body alignment of point cloud, projection transformations and elastic transformations, etc.

3.2. *Point cloud rigid body alignment modeling*

The rigid-body transformation of a point cloud is an important basis for the non-rigid-body transformation, and the alignment model established by the rigid-body transformation between two groups of point clouds is called the rigid-body alignment of the point cloud, and the parameters to be solved for in the rigid-body alignment mainly include the rotation matrix R and the translation vector t. For two groups of point clouds in the R^m-space, the shape cloud S and the model cloud M, assuming that there are any two points x and $y, x \in S, y \in M$, then the rigid-body transformation takes the specific form of:

$$y = Rx + t \tag{10}$$

Eq:

R - $m \times m$-dimensional rotation matrix;

t - $m \times 1$-dimensional translation vector. The two sets of point clouds are accomplished by means of rigid-body transformations, in which the representation of the rotation matrix R is currently dominated by the Euler angle, quaternion, orthogonal matrix, and perimeter angle methods, among others. The Euler angle method is introduced below:

The alignment process of the point cloud is set to be H represented by the mapping transformation, H as:

$$H = \begin{bmatrix} a_{11} & a_{12} & a_{13} & t_x \\ a_{21} & a_{22} & a_{23} & t_y \\ a_{31} & a_{32} & a_{33} & t_z \\ v_x & v_y & v_z & s \end{bmatrix} \tag{11}$$

It can also be simplified and expressed as:

$$H = \begin{bmatrix} A & t \\ V & s \end{bmatrix} \tag{12}$$

Eq:

$A = \begin{bmatrix} a_{11} & a_{12} & a_{13} \\ a_{21} & a_{22} & a_{23} \\ a_{31} & a_{32} & a_{33} \end{bmatrix}$ - rotation matrix

$t = \begin{bmatrix} t_x & t_y & t_z \end{bmatrix}^T$ - rotation matrix.

$V = \begin{bmatrix} V_x & V_y & V_z \end{bmatrix}$ - Perspective transformation vector;

s - overall scale factor.

There is no deformation in the rigid body transformation, so it is expressed as:

$$H = \begin{bmatrix} R_{m\times m} & t_{m\times 1} \\ \theta_{1\times m} & s \end{bmatrix} \tag{13}$$

where the rotation matrix $R_{m\times m}$ and translation matrix $t_{m\times 1}$ are denoted as:

$$R_{m\times m} = \begin{bmatrix} 1 & 0 & 0 \\ 0 & \cos\alpha & \sin\alpha \\ 0 & -\sin\alpha & \cos\alpha \end{bmatrix} \begin{bmatrix} \cos\beta & 0 & -\sin\beta \\ 0 & 1 & 0 \\ \sin\beta & 0 & \cos\beta \end{bmatrix} \begin{bmatrix} \cos\gamma & \sin\gamma & 0 \\ -\sin\gamma & \cos\gamma & 0 \\ 0 & 0 & 1 \end{bmatrix} \tag{14}$$

$$t_{m\times 1} = \begin{bmatrix} t_x & t_y & t_z \end{bmatrix}^T \tag{15}$$

Where: α, β, γ is the rotation angle along the x, y, z -axis, respectively; and t_x, t_y, t_z is the translation vector along the x, y, z -axis, respectively.

Coordinate transformations are performed on the two sets of point clouds:

$$x' = Rx + t \tag{16}$$

Can be obtained by substituting x and x' respectively into Eq:

$$\begin{bmatrix} x_{i'} \\ y_{i'} \\ z_{i'} \end{bmatrix} = \begin{bmatrix} 1 & 0 & 0 \\ 0 & \cos\alpha & \sin\alpha \\ 0 & -\sin\alpha & \cos\alpha \end{bmatrix} \begin{bmatrix} \cos\beta & 0 & -\sin\beta \\ 0 & 1 & 0 \\ \sin\beta & 0 & \cos\beta \end{bmatrix} \begin{bmatrix} \cos\gamma & \sin\gamma & 0 \\ -\sin\gamma & \cos\gamma & 0 \\ 0 & 0 & 1 \end{bmatrix} \begin{bmatrix} x_i \\ y_i \\ z_i \end{bmatrix} + \begin{bmatrix} t_x \\ t_y \\ t_z \end{bmatrix} \tag{17}$$

The rotation matrix $R_{m\times m}$ can be finally expressed as:

$$R_{m\times m} = \begin{bmatrix} \cos\beta\cos\gamma & \cos\beta\sin\gamma & -\sin\beta \\ -\cos\alpha\sin\gamma - \sin\alpha\sin\beta\cos\gamma & \cos\alpha\cos\gamma + \sin\alpha\sin\beta\sin\gamma & \sin\alpha\cos\beta \\ \sin\alpha\sin\gamma + \cos\alpha\sin\beta\cos\gamma & -\sin\alpha\cos\gamma - \cos\alpha\sin\beta\sin\gamma & \cos\alpha\cos\beta \end{bmatrix} \tag{18}$$

There are six unknowns in the mathematical model of rigid-body transformation $\alpha, \beta, \gamma, t_x, t_y, t_z$, then 3 sets of non-collinear corresponding points need to be found in the overlapping region of the point cloud to be aligned in order to solve for the values of the unknowns. It is worth mentioning that in the point cloud rigid-body alignment, due to the existence of the constraints in R, R can be expressed by the Euler angles, while the affine transformation cannot. In order to estimate the parameter values more accurately, as many pairs of points as possible should be selected to further improve the accuracy of the point cloud alignment.

3.3. *Improved RANSAC point cloud segmentation algorithm*

Most of the papers select the height threshold is set manually, which is cumbersome and not easy to obtain the optimal segmentation results. This chapter will make a detailed introduction around the key techniques involved in the process of the middle RANSAC [42] and the optimization algorithm process.

3.3.1. Basic flow framework of the algorithm. Aiming at the defects caused by the RANSAC fitting segmentation process, an adaptive hyperparametric RANSAC segmentation algorithm is proposed.

First, the initial point cloud data octree voxelized.

Second, input the point cloud data.

Third, enter k algorithmic cycles to fit segmentation to the point cloud data.

Fourth, calculate the dynamic height h to set the threshold.

Fifth, calculate the normal vectors between the consensus surfaces and determine the size of the normal vector angle threshold.

Sixth, the final consensus facets are input and marked by color descending.

Seventh, the unfitted points are extracted into the same set, the Euclidean distance is calculated, the minimum distance is selected, and the points are merged with respect to the nearest planes if they are within the threshold to get the final result.

3.3.2. Spatial structure representation of point cloud algorithms. In this paper, the octree is selected to spatialize the point cloud, and the process of octree voxelization of point cloud data in this paper is: 1) First determine the maximum depth of the enclosing box and the octree, and determine the maximum values $(x_{\max}, y_{\max}, z_{\max})$ and $(x_{\min}, y_{\min}, z_{\min})$ of the direction where x, y, z is located under the three-dimensional coordinate system in the data. Calculate the lengths of the three sides of the voxel separately, by means of Eq:

$$len_a = | a_{\max} - a_{\min} | (a = x, y, z) \tag{19}$$

2) Determine the coordinates of the root node of the octree, calculated as:

$$\left(x_{\min} + \frac{len_x}{2}, y_{\min} + \frac{len_y}{2}, z_{\min} + \frac{len_z}{2} \right) \tag{20}$$

3) Recursive octree. Set up the spatial coordinate system and set the root node of the spatial coordinate system as the origin.
4) Store points. After the construction of the octree is completed, calculate the spatial coordinates to judge with the sub-enclosure box to decide into which voxel the point is placed.

In this paper, the center of gravity distance of the octree is combined with the normal vector to downsample the point cloud data.

(1) Point cloud center of gravity. After obtaining the coordinates of the center of gravity point in the voxel, we can traverse the data and calculate the distance between the point coordinate C and the center of gravity P in the 3D point cloud data in the voxel, the formula is:

$$\bar{a} = \frac{1}{n} \sum_{i=0}^{n} C_{ia} (a = x, y, z) \tag{21}$$

(2) Normal vector calculation. In this paper, the normal vector calculation of the fitting plane should ensure that the center of gravity P is above the set fitting plane, and the calculation of the normal vector can be divided into the following operation steps:

(a) First, the set of points in the voxel is transformed into matrix E form to form the space of $n*3$. Each row corresponds to the coordinates of the point cloud within the voxel as follows:

$$E = \begin{bmatrix} x_1, y_1, z_1 \\ x_2, y_2, z_2 \\ \cdots \\ x_n, y_n, z_n \end{bmatrix} \tag{22}$$

(b) Next the matrix E is decentered and the decentered matrix can be represented by the following:

$$E' = \begin{bmatrix} x_1 - x_i, y_1 - y_i, z_1 - z_i \\ x_2 - x_i, y_2 - y_i, z_2 - z_i \\ \cdots \\ x_n - x_i, y_n - y_i, z_n - z_i \end{bmatrix} \tag{23}$$

(c) Calculate the covariance matrix, and also calculate the eigenvalues and eigenvectors of the covariance matrix.

3) Calculation of residual values. The normal vector and the fitted plane obtained by passing through the center of gravity point have been obtained, so now the residual value can be calculated to obtain the corresponding distance to do downsampling operations on the data model. The data size of the residual value is proportional to the noise distribution and surface curvature of the plane, and the calculation formula is shown below:

$$l=\sqrt{\frac{1}{n}\sum_{i=1}^{n}\frac{\left|Ax_i+By_i+Cz_i+D\right|^2}{A^2+B^2+C^2}} \tag{24}$$

After calculating the distance l between each point and the fitting plane, the mean residual value distance is obtained, and the operation of downsampling within voxels is completed by eliminating the points smaller than the mean value by calculating the distance between each point and the fitting plane.

After the downsampling process is completed, the next step is to make improvements to the RANSAC segmentation process.

3.3.3. Parameter-adaptive RANSAC algorithm. This paper focuses on the improvement of the hyperparametric RANSAC algorithm. The initial point cloud data has now been given a new model of the processed voxel downsampling. On this basis this point cloud data is segmented using the improved RANSAC fitting algorithm.

Within a reasonable range, an iterative approach is used to fuse the eligible point cloud data into the fitting surface S to achieve the fitting operation on the dataset within the range, which is an important step in fitting segmentation.

The process of selecting seed points is operated using the farthest point sampling method.

The FPS (Farthest Point Sampling) algorithm searches for the farthest point in a point. The specific process is as follows:

1) Set the number of point clouds in the point cloud dataset as N. Firstly, a point Q_1 in the point cloud data is randomly determined, and the distance value d is calculated between the Q_1 point and the other $N-1$ points in the model, and after comparing and sorting, the seed point with the largest distance value is selected Q_2. The formula for calculating the distance of the point in the space is as follows:

$$d=\sqrt{(x_1-x_2)^2+(y_1-y_2)^2+(z_1-z_2)^2} \tag{25}$$

2) After comparing the point spacing $(d_1,d_2,...d_{n-2})$ again in descending order, the farthest point Q_3 can be obtained.

The initial god sub-points selected with this method can ensure that its initial selection of the point composition of the maximum area, which in turn can improve the accuracy of the fitted plane. The triangular composition area can be obtained by utilizing the Helen formula:

$$S=\sqrt{p(p-a)(p-b)(p-c)} \tag{26}$$

a,b,c are the lengths of the three sides of the triangle, respectively, and are obtained on the computation of p :

$$p=(a+b+c)/2 \tag{27}$$

Therefore the obtained triangular area is subjected to a limiting judgment with hyperparameters in order to satisfy that the obtained fitted surface meets the preset selected conditions, and the next step is the process of calculating the adaptive parameters.

The seed point $Q_1(x_1,y_1,z_1),Q_2(x_2,y_2,z_2),Q_3(x_3,y_3,z_3)$ has been selected in the above process by combining the FPS algorithm. The corresponding coefficients of plane S are determined through the fitting plane formed by the three points as follows:

$$S = Ax + By + Cz + D \tag{28}$$

After determining the consensus surface, the coordinate dependent equations are determined as follows:

$$\begin{bmatrix} x-x_1, y-y_1, z-z_1 \\ x_2-x_1, y_2-y_1, z_2-z_1 \\ x_3-x_2, y_3-y_2, z_3-z_2 \end{bmatrix} \tag{29}$$

After determining the coordinate dependent equations, the value of A,B,C can be obtained by matrix substitution with the following matrix coefficient formula:

$$A = y_1z_2 + y_2z_1 + y_2z_3 - y_3z_2 - y_2z_1 - y_1z_3 \tag{30}$$

$$B = x_3z_2 + x_2z_1 + x_1z_3 - x_1z_2 - x_3z_1 - x_2z_3 \tag{31}$$

$$C = x_1y_2 + x_3y_1 + x_2y_3 - x_3y_2 - x_2y_1 - x_1y_3 \tag{32}$$

After calculating the A,B,C, you can then obtain the D value, which can be derived by combining the three values from the matrix as follows:

$$D = x_3y_2z_1 + x_2y_1z_3 + x_1y_3z_2 - x_1y_2z_3 - x_3y_1z_2 - x_2y_3z_1 \tag{33}$$

After obtaining the formula for S, the distance is calculated for the points within the threshold range of the consensus surface, yielding the distance between each point and the fitted surface, and the formula for calculating the distance is as follows:

$$d = \frac{Ax_Q + By_Q + Cz_Q + D}{\sqrt{A^2 + B^2 + C^2}} \tag{34}$$

The dynamic threshold d_k is calculated as follows:

1) First the standard deviation of all points to the fitting surface S, where d_i is the point-by-point point spacing and N is the number of point clouds.

$$\theta = \sqrt{\frac{\sum_{i=1}^{N}(d_i - \bar{d})^2}{N-1}} \tag{35}$$

2) The calculation for $\bar{d}$ can be obtained by averaging the distance d cumulatively with the following formula:

$$\bar{d} = \frac{1}{N}\sum_{i=1}^{N} d_i \tag{36}$$

The essence of the RANSAC fitting segmentation algorithm is to extract as much as possible from a noisy dataset, and is therefore inherently stochastic and hypothetical. The underlying judgment is shown below:

$$1-(1-\xi^n)^k > P_0 \tag{37}$$

Threshold $E(k)$. After iteration, the model with the largest percentage of proportional size is taken as the best model, i.e., the best plane of mathematical fit with the highest degree of practical agreement, calculated as follows:

$$k = \log(1-P_0)/\log(1-\xi^n) \tag{38}$$

The standard deviation is calculated as follows:

$$S(k) = \sqrt{1-\xi^n}\ /\ \xi^n \tag{39}$$

The final number of iterations can be obtained by summing:

$$E(k) = k + S(k) \tag{40}$$

The next operation of merging the facets of the fitted facets that meet the angular threshold range is the last step of the main flow of the RANSAC algorithm.

The effect of plane over-segmentation is eliminated by merging the facets, and the magnitude of the angle between the fitted facets S_1 and S_2 is calculated using the geometric normal vectors $\vec{n_1}$ and $\vec{n_2}$. The computational metrics for the angle are as follows:

$$\theta = \arccos^{-1}(\overline{n_1} \cdot \overline{n_2}) \tag{41}$$

The formula for the distance between interplanar faces is calculated, but the angle calculated by this law increases proportionally to the size of the distance from the point to the plane, which in turn leads to large fluctuations in the distance to the face piece obtained from different normal vectors. The distance formula is as follows:

$$l = \max|\overline{r_{12}} \cdot \overline{n_1}|,|\overline{r_{12}} \cdot \overline{n_2}|) \tag{42}$$

The two slices can be merged when considered within a threshold that simultaneously meets the angle and distance.

3.3.4. Secondary Point Cloud Fitting Surface Merging. The objective of the secondary fitting of the RANSAC segmentation algorithm is to reduce the unfit rate, so based on the primary fitting, a secondary merging process operation is done on the nearest fitted surface within the threshold range of the untreated points.

4. Example analysis of bridge monitoring

Quality assessment and screening of dynamic monitoring data of a large-span cable-stayed bridge in A city. The main span of the bridge is (40 + 80 + 250 + 80 + 40) m, and it is a double-tower transverse steel box girder semi-floating system. The bridge dynamic monitoring signal sensors can collect about 600 data per day, including 8 tension cable vibration sensors with a sampling frequency of 33 Hz, and 16 main girder vibration sensors with a sampling frequency of 32 Hz.

4.1. Fit of RANSAC algorithm to point cloud data

We planned and implemented the collection of building point cloud data. A total of 18 sites were set up around the building, and the distribution of the sites is shown in Fig. 2. The spacing of the sites is about 4-8 meters, and the overlap rate is 43%-68%. In particular, in the first floor, we set site 19 as an indoor-outdoor contact point for completing the stitching of point cloud data inside and outside the building, so that the preprocessing and quality checking of point cloud data inside and outside the building can be completed at one time. A total of 18 sites are set up on each floor of the building. The spacing of each site is about 3.3-8 meters, and the overlap rate is 30%-62%.

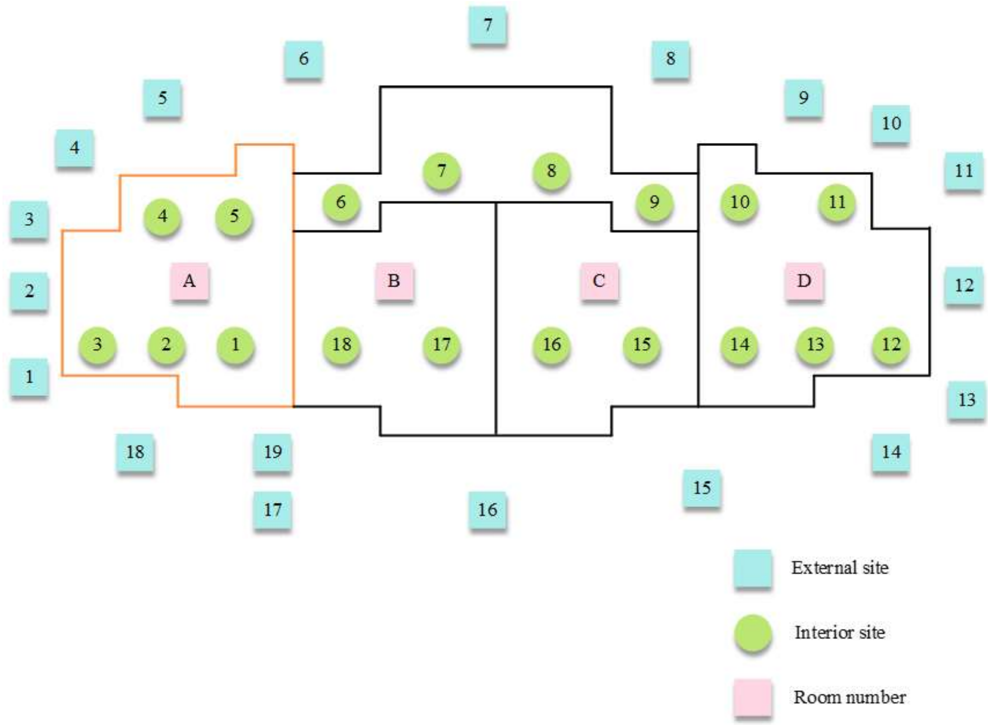

Fig. 2. Interior and external site diagram

Using the improved RANSAC algorithm for feature extraction and fitting of point cloud data, selected part of the bridge bearing for the index calculation work, in order to compare, we used the traditional ruler measurement method and the plane fitting method based on the improved RANSAC point cloud segmentation algorithm, respectively, to carry out the construction quality inspection of the walls of each side of the two bedrooms, and the results of the experimental data are shown in Table 1. The tested bridge bearing indicators can meet the requirements of the quality inspection standards. The flatness error of the bearing 3 under the detection of this paper's method is improved by 78.26% compared with the traditional monitoring method. Among them, the bearing 4 has a large deviation from the indicators, which can be adjusted appropriately so as to improve the overall quality and durability of the bridge building.

The difference between the detection results of the traditional footing method and the plane-fitting method is diametrically opposite in the cross-section dimensions and other indexes, and the traditional footing method is usually larger than the plane-fitting method in the cross-section dimensions detection results, but smaller than the latter in the flatness and perpendicularity detection results. This phenomenon can be attributed to two reasons, on the one hand, in the dimensional inspection, the manually placed measuring tape is difficult to be completely parallel to the measured surface, resulting in large ruler measurement data. On the other hand, in the flatness and perpendicularity inspection, the measuring tape placed during manual inspection is subjectively influenced by the workers, and the measured value only indicates the result at the point where the measuring tape is placed, which leads to a smaller result in the ruler measurement.

Table 1. Bridge support test results

Detection index	Section size		Smoothness		Perpendicularity	
Permissible error	+10	-5	8		10	
Model	Traditional	Textual	Traditional	Textual	Traditional	Textual

Support1	4002*2902	4002*2897	2.82	2.62	3.51	3.64
Support2	6304*2897	6301*2903	2.12	2.94	1.03	2.23
Support3	4001*2905	4003*2902	1.84	3.28	2.54	1.93
Support4	6301*2903	6298*2894	4.56	3.89	4.55	6.44

Then the flatness and perpendicularity of each bearing of the bridge are analyzed in detail, Fig. 3-Fig. 6 shows the distribution of the distance between the point cloud data and the fitting plane of each bearing, it can be seen that there is a small part of point cloud exceeding the maximum allowable deviation range in each bearing, we have counted the number of point cloud exceeding the maximum allowable deviation in each bearing, and the results show that in the bearings 1 to 4, there are 1.36% respectively, 1.64%, 1.82%, and 2.25% of the point clouds exceeded the limit values and were within the maximum allowable deviation.

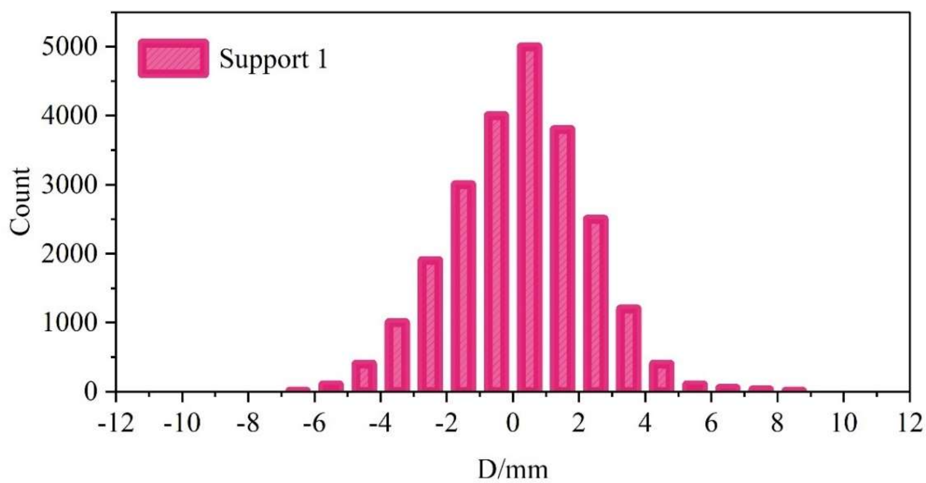

Fig. 3. Dot cloud distribution statistics of support 1

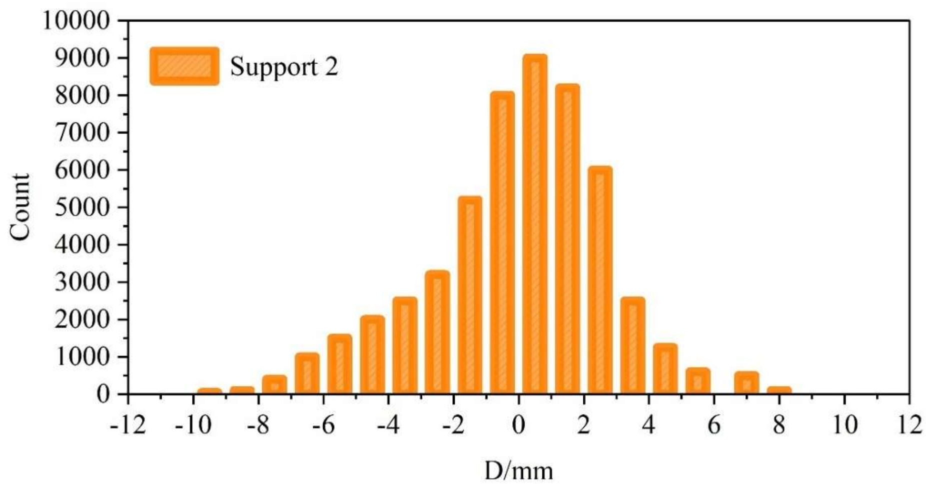

Fig. 4. Dot cloud distribution statistics of support 2

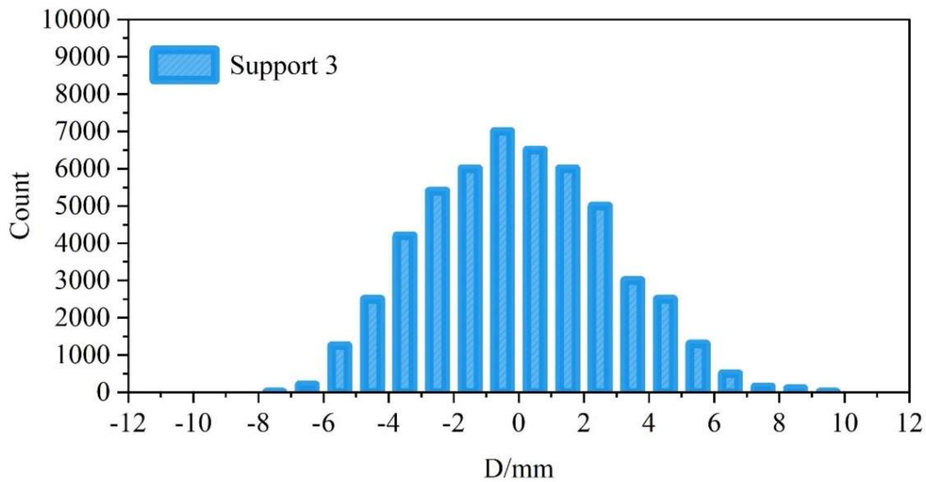

Fig. 5. Dot cloud distribution statistics of support 3

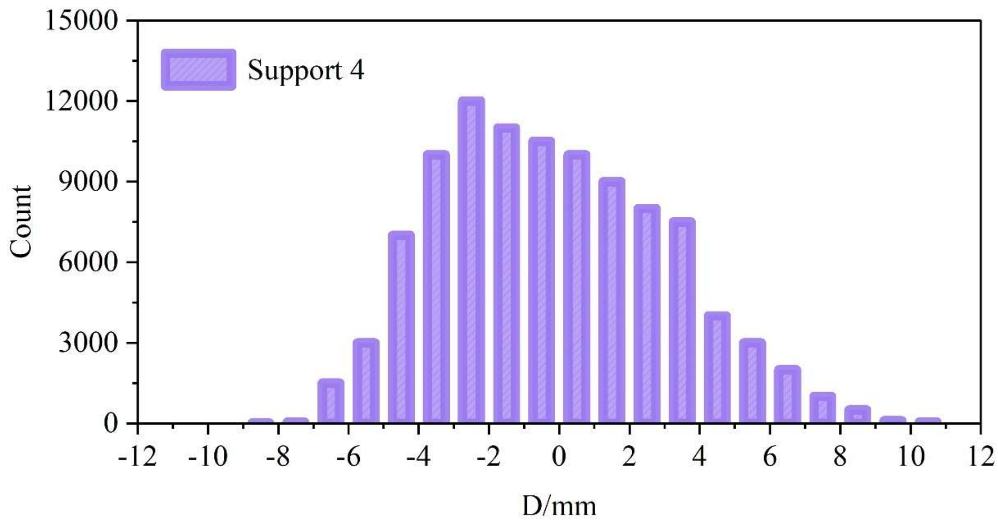

Fig. 6. Dot cloud distribution statistics of support 4

4.2. Effectiveness of RANSAC algorithm for fitting point cloud data

Comparison and analysis of 3D point cloud and design model is a great advantage of 3D laser scanning technology for structural inspection, and its advancement over traditional measurement and comparison methods is reflected in the huge number of point clouds scanned by 3D laser scanning, which is not realized by manual measurement. Thanks to the dense three-dimensional point cloud, the contour of the components can be fully mapped, especially the shaped, curved irregular components are more accurate, and the scanning accuracy is more stable and accurate compared to manual measurement. Based on the fine mapping of the 3D point cloud on the contour of the components, its comparative analysis with the design model can fully demonstrate the real state of each part of the components on site, as well as accurately calculate the error with the design model, providing real and effective reference data for the designers.

Through the software annotation function to extract the vertical frame of the lower support, the upper support and the corner of the offset, and output reports. The offset statistics of the lower support, upper support and corner point of the vertical frame are shown in Table 2-Table 4 respectively.

Lower bearing node offset is measured in the outermost horizontal section of the offset, the data looks like the overall upward offset, there are two possibilities: one is the deviation of the release line, and the other is that the member of the point for the inflection point, the collation of the data may be positioned will be biased upward.

Upper bearing are the existence of vertical section of steel members, only X, Y coordinates of the results of the collation (Z coordinates have no effect on the calculation, the length of the vertical section does not affect the force); upper bearing positioning is more accurate, the deviation is small.

A total of 20 bridge members were tested for corner point offset, with no deviation above 70cm. The deviation of 50~70cm is 2 for S1 and S32, and the deviation of 30~50cm is 6 for S9, S11, S13, S16, S30, S34, S36, and S38. The maximum deviation of the corner offset of the measured bridge building is only 0.623m, which is within the acceptable error range.

Table 2. Offset of lower support

Serial number	Test axis number	Offset/m		
		ΔX	ΔY	ΔZ
1	S1	0.039	-0.751	0.309
2	S3	0.079	-0.249	0.4
3	S5	0.323	-0.681	0.319
4	S7	0.464	-0.591	0.295
5	S9	0.564	-0.493	0.318
6	S11	0.66	-0.363	0.325
7	S13	0.222	-0.063	0.445
8	S15	0.751	0.011	0.279
9	S16	0.751	0.091	0.326
10	S18	0.209	0.088	0.442
11	S20	0.649	0.378	0.312
12	S22	0.554	0.512	0.287
13	S24	0.444	0.606	0.339
14	S26	0.308	0.688	0.339
15	S28	0.022	0.24	0.411
16	S30	0.025	0.749	0.311
17	S32	-0.079	0.199	0.432
18	S34	-0.125	0.212	0.42
19	S36	-0.43	0.615	0.208
20	S38	-0.549	0.515	0.299

Table 3. Upper support offset

Serial number	Test axis number	Offset/m	
		ΔX	ΔY
1	S1	-0.014	0.047
2	S3	0.017	0.047
3	S5	-0.01	0.03
4	S7	-0.027	0.043
5	S9	0.04	0.031
6	S11	-0.043	0.042
7	S13	-0.051	0.037
8	S15	-0.057	0.028
9	S16	-0.035	0.026
10	S18	0.08	0.038
11	S20	-0.032	0.019
12	S22	-0.035	0.038
13	S24	-0.027	0.012
14	S26	-0.009	0.023
15	S28	-0.037	0.012
16	S30	-0.015	0.009

17	S32	-0.018	0.022
18	S34	-0.017	0.027
19	S36	0.032	-0.016
20	S38	0.022	-0.017

Table 4. Angle offset

Serial number	Test axis number	Offset/m			
		ΔX	ΔY	Plane displacement	ΔZ
1	S1	-0.577	0.227	0.623	-0.119
2	S3	-0.104	0.224	0.249	-0.036
3	S5	-0.095	0.185	0.208	0.049
4	S7	-0.114	0.264	0.286	-0.078
5	S9	-0.214	0.221	0.302	0.047
6	S11	-0.217	0.247	0.328	-0.005
7	S13	-0.193	0.356	0.402	-0.048
8	S15	-0.275	-0.031	0.274	-0.068
9	S16	-0.245	-0.343	0.420	-0.093
10	S18	-0.212	-0.135	0.256	0.017
11	S20	-0.144	-0.267	0.299	-0.008
12	S22	-0.282	-0.036	0.285	0.045
13	S24	-0.246	-0.104	0.264	0.002
14	S26	-0.126	-0.207	0.246	0.043
15	S28	-0.027	-0.278	0.287	-0.002
16	S30	0.236	-0.308	0.389	-0.039
17	S32	0.573	-0.267	0.632	-0.116
18	S34	0.33	-0.154	0.363	-0.102
19	S36	0.02	-0.425	0.425	-0.082
20	S38	0.388	0.075	0.395	-0.096

4.3. Bridge quality monitoring point cloud data analysis

In this paper, for the characteristics of the vibration monitoring data of cable-stayed bridges, the histogram KL dispersion, the histogram cosine value and the percentage of normal value of the box-and-line diagram are selected as the data quality assessment indicators, and the quantitative standards of the indicators are shown in Table 5. It is worth noting that the calculation results of the indicators are affected by abnormal data to a certain extent, so the set thresholds do not fully correspond to the actual quality level of the data, and there are cases in which the evaluation results of individual indicators do not match the actual quality.

Table 5. Data quality quantification standard

Inspection standard	Histogram		The normal data ratio of the box diagram
	Kl divergence	Cosine similarity	
Excellence	[0.00,0.10)	(0.95,1.00]	(0.95,1.00]
Good	[0.10,0.15)	(0.95,0.95]	(0.95,0.95]
Bad	⩾0.15	⩽0.90	⩾0.90

To test whether the data obey normal distribution, in addition to the method through this paper, can also be through the skewness, kurtosis, and Shapiro-Wilk test and other statistical indicators.Shapiro-Wilk test is usually only applicable to the case of small sample capacity ($8 \leqslant n \leqslant 50$), when the sample capacity is larger is prone to significance problems. Whereas kurtosis and skewness can be used for cases with larger sample capacity. In addition, for the rapid detection of data anomalies, there are methods such as the 3ρ criterion, which defines data points outside the interval of the mean plus or minus three times the standard deviation as outliers. In summary, the kurtosis, skewness and 3ρ criterion are compared with the method proposed by the author, and 2,000 data each of the vibration acceleration of the main beam of the sensor of the bridge numbered 1 are selected, and the histograms, Q-Q plots, and box plots plotted are shown in Figs. 7-Fig. 9, respectively.

The actual distribution function of the histogram of the acceleration data of the sensor numbered 1 roughly coincides with that of the normal fit function, and the scatter points of the Q-Q plot are approximately distributed on the quartile straight line with deviations at both ends. The boxplot data distribution is symmetric along the value of 0, and the percentage of normal data is 0.993. Therefore, the acceleration data of sensor No. 1 is evaluated as of excellent quality, and since the Q-Q plot scatter is deviated greatly at both ends, the histogram KL scatter, histogram cosine, and the boxplot are still selected as the evaluation indexes under the quality monitoring of bridges in this paper.

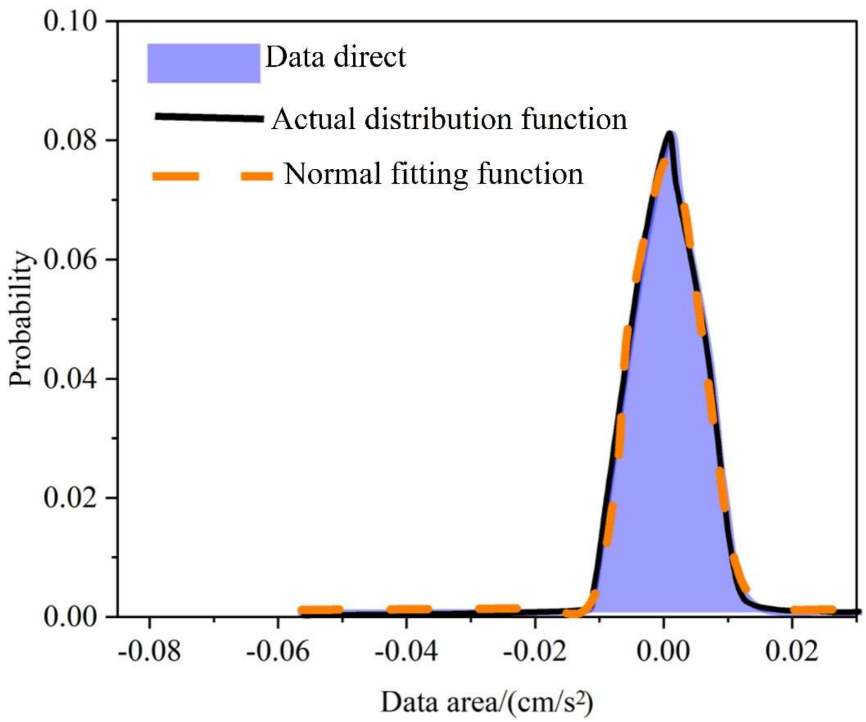

Fig. 7. Histogram

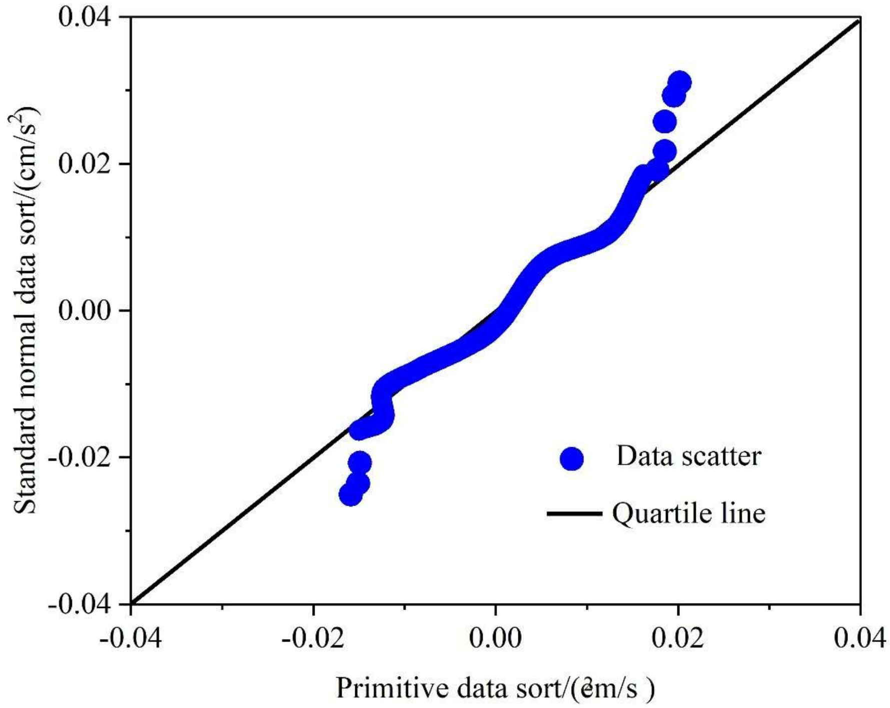

Fig. 8. Q-Q diagram

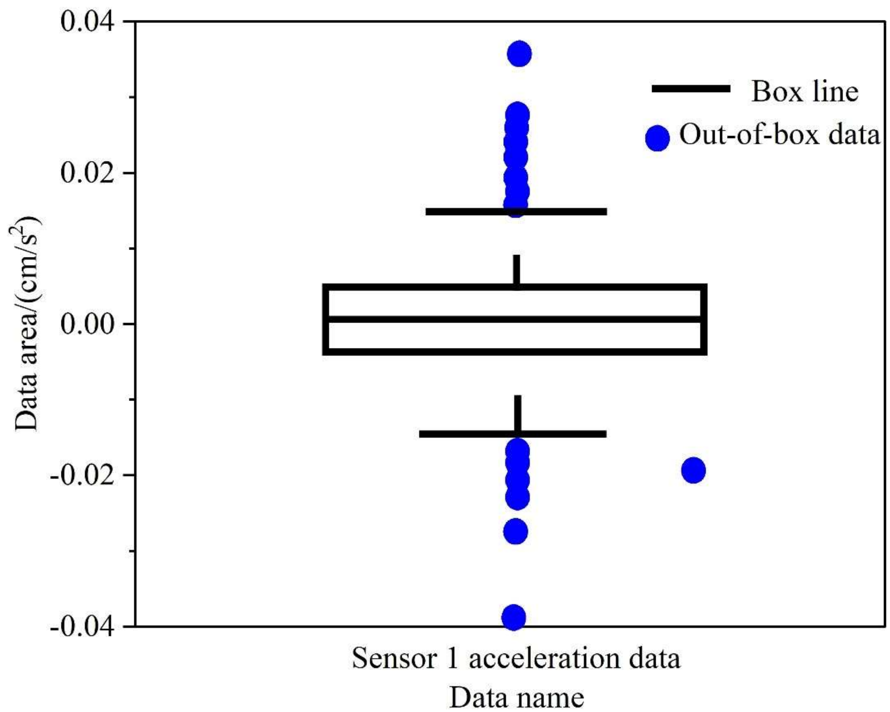

Fig. 9. Box diagram

The histogram KL value and cosine similarity were used as the main indicators, and the box-and-line plot normal value percentage was used as the auxiliary indicator to automatically assess and filter the quality of the dynamic monitoring data of the bridge. Each sensor data is divided into 1400 segments by 1min unit, and three quantitative indexes are calculated for each segment of data, and the statistical results are shown in Table 6. The quality of the structural vibration data of the main girder of the bridge is relatively good, but the superiority rate of the sensor numbered Z006 is only 19.64%, which is a large gap with the monitoring data of other sensors, and it is recommended to check whether there is an interference source near the sensors with generally poor data quality, or whether the sensors have been malfunctioning.

Table 6. Acceleration data quality rating

Sensor number	Number of levels of data			Rate of excellence/%	Overall quality
	Excellence	Good	Bad		
Z001	769	445	186	54.93	Excellence
Z002	532	748	120	38.00	Good
Z003	1135	210	55	81.07	Excellence
Z004	436	682	282	31.14	Good
Z005	275	483	642	19.64	Bad
Z006	487	617	296	34.79	Good

5. Conclusion

This paper proposes an improved parameter-adaptive RANSAC segmentation algorithm based on laser point cloud technology, based on which the quality detection of bridges is analyzed in a more systematic way.

This paper develops a three-dimensional laser scanning based construction bridge quality detection method, through the analysis of the relationship between the fitting plane and the point cloud data, effectively and reliably complete the quality detection of the bridge, the accuracy of the work is improved compared with the traditional detection methods, the accuracy of the detection of the leveling of the bearing of the bridge No. 3 under the method of this paper is improved by 78.26%. Provides strong support for the workers' subsequent construction link intelligence, and promotes the intelligent development of bridge construction engineering.

Error analysis is performed on the offset data of the lower support, upper support and corner points of the monitored bridge. The offset of the corner point of the bridge structure detected by the method of this paper did not appear above 70cm, and the maximum offset of the measured corner point of the bridge building was only 0.623m, which is within the acceptable range of the bridge error monitoring. The feasibility of bridge quality inspection by laser point cloud technology is verified.

Finally, the histogram KL dispersion and cosine similarity are selected as the main indexes of bridge quality assessment, and the quality monitoring of a large-span cable-stayed bridge in A city is found that the structural vibration data of the main girder of the bridge is of better quality, and the method of this paper better realizes the dynamic monitoring of the bridge quality.

References

[1] He, X., Wu, T., Zou, Y., Chen, Y. F., Guo, H., & Yu, Z. (2017). Recent developments of high-speed railway bridges in China. Structure and Infrastructure Engineering, 13(12), 1584-1595.

[2] Qin, S., & Gao, Z. (2017). Developments and prospects of long-span high-speed railway bridge technologies in China. Engineering, 3(6), 787-794.

[3] Jeong, Y., Kim, W., Lee, I., & Lee, J. (2017). Bridge service life estimation considering inspection reliability. KSCE Journal of Civil Engineering, 21, 1882-1893.

[4] Xu, S., Wang, J., Wang, X., Shou, W., & Ngo, T. (2024). Defect modelling and correlation mapping for bridge inspection. Engineering, Construction and Architectural Management.

[5] Washer, G. A., Hammed, M. M., Jensen, P., & Connor, R. J. (2020). Quality of element-level bridge inspection data. Transportation Research Record, 2674(2), 252-261.

[6] Wójcik, B., & Żarski, M. (2020). Asesment of state-of-the-art methods for bridge inspection: case study. Archives of Civil Engineering, 66(4).

[7] Abdelkhalek, S., & Zayed, T. (2020). Comprehensive inspection system for concrete bridge deck application: Current situation and future needs. Journal of Performance of Constructed Facilities, 34(5), 03120001.

[8] Khedmatgozar Dolati, S. S., Caluk, N., Mehrabi, A., & Khedmatgozar Dolati, S. S. (2021). Non-destructive testing applications for steel bridges. Applied Sciences, 11(20), 9757.

[9] La, H. M., Gucunski, N., Kee, S. H., & Nguyen, L. V. (2015). Data analysis and visualization for the bridge deck inspection and evaluation robotic system. Visualization in Engineering, 3, 1-16.

[10] An, Y., Chatzi, E., Sim, S. H., Laflamme, S., Blachowski, B., & Ou, J. (2019). Recent progress and future trends on damage identification methods for bridge structures. Structural Control and Health Monitoring, 26(10), e2416.

[11] Zanini, M. A., Faleschini, F., & Casas, J. R. (2019). State-of-research on performance indicators for bridge quality control and management. Frontiers in built environment, 5, 22.

[12] Xin, J., Wang, C., Tang, Q., Zhang, R., & Yang, T. (2023). An evaluation framework for construction quality of bridge monitoring system using the DHGF method. Sensors, 23(16), 7139.

[13] Lee, J. K., Lee, J. O., & Kim, J. O. (2016). New quality control algorithm based on GNSS sensing data for a bridge health monitoring system. Sensors, 16(6), 774.

[14] Truong-Hong, L., & Laefer, D. F. (2019). Laser scanning for bridge inspection. In Laser Scanning (pp. 189-214). CRC Press.

[15] Wang, D., Gao, L., Zheng, J., Xi, J., & Zhong, J. (2025). Automated recognition and rebar dimensional assessment of prefabricated bridge components from low-cost 3D laser scanner. Measurement, 242, 115765.

[16] Owerko, P., & Owerko, T. (2020). Novel approach to inspections of as-built reinforcement in incrementally launched bridges by means of computer vision-based point cloud data. IEEE Sensors Journal, 21(10), 11822-11833.

[17] Hodge, G., & Gattas, J. M. (2022). Geometric and semantic point cloud data for quality control of bridge girder reinforcement cages. Automation in Construction, 140, 104334.

[18] Rashidi, M., Mohammadi, M., Sadeghlou Kivi, S., Abdolvand, M. M., Truong-Hong, L., & Samali, B. (2020). A decade of modern bridge monitoring using terrestrial laser scanning: Review and future directions. Remote Sensing, 12(22), 3796.

[19] Li, J., Peng, Y., Tang, Z., & Li, Z. (2023). Three-Dimensional Reconstruction of Railway Bridges Based on Unmanned Aerial Vehicle–Terrestrial Laser Scanner Point Cloud Fusion. Buildings, 13(11), 2841.

[20] Truong-Hong, L., & Lindenbergh, R. (2022). Automatically extracting surfaces of reinforced concrete bridges from terrestrial laser scanning point clouds. Automation in Construction, 135, 104127.

[21] Hosamo, H. H., & Hosamo, M. H. (2022). Digital twin technology for bridge maintenance using 3d laser scanning: A review. Advances in Civil Engineering, 2022(1), 2194949.

[22] Chen, S., Laefer, D. F., Mangina, E., Zolanvari, S. I., & Byrne, J. (2019). UAV bridge inspection through evaluated 3D reconstructions. Journal of Bridge Engineering, 24(4), 05019001.

[23] Li, S., Zhang, B., Zheng, J., Wang, D., & Liu, Z. (2024). Development of Automated 3D LiDAR System for Dimensional Quality Inspection of Prefabricated Concrete Elements. Sensors, 24(23), 7486.

[24] Yan, Y., & Hajjar, J. F. (2021). Automated extraction of structural elements in steel girder bridges from laser

point clouds. Automation in Construction, 125, 103582.

[25] Castellani, M., Meoni, A., García-Macías, E., Antonini, F., & Ubertini, F. (2024). UAV photogrammetry and laser scanning of bridges: a new methodology and its application to a case study. Procedia Structural Integrity, 62, 193-200.

[26] Valença, J., Puente, I., Júlio, E. N. B. S., González-Jorge, H., & Arias-Sánchez, P. (2017). Assessment of cracks on concrete bridges using image processing supported by laser scanning survey. Construction and Building Materials, 146, 668-678.

[27] Maizuar, M., Zhang, L., Miramini, S., Mendis, P., & Thompson, R. G. (2017). Detecting structural damage to bridge girders using radar interferometry and computational modelling. Structural Control and Health Monitoring, 24(10), e1985.

[28] Zhang, G., Cheng, Y., Xia, Q., & Zhang, J. (2023). Curvature envelope area based rapid identification method of bridge distributional element stiffness using microwave interference radar. Mechanical Systems and Signal Processing, 197, 110390.

[29] Yaghoubzadehfard, A., Lumantarna, E., Herath, N., Sofi, M., & Rad, M. (2024). Ensemble learning-based structural health monitoring of a bridge using an interferometric radar system. Journal of Civil Structural Health Monitoring, 1-22.

[30] Mizutani, T., Nakamura, N., Yamaguchi, T., Tarumi, M., Ando, Y., & Hara, I. (2017). Bridge slab damage detection by signal processing of UHF-band ground penetrating radar data. Journal of Disaster Research, 12(3), 415-421.

[31] Baba, S., & Kondoh, J. (2022). Damage evaluation of fixed beams at both ends for bridge health monitoring using a combination of a vibration sensor and a surface acoustic wave device. Engineering Structures, 262, 114323.

[32] Mahvelati, S., & Coe, J. T. (2017). The use of two dimensional (2D) multichannel analysis of surface waves (MASW) testing to evaluate the geometry of an unknown bridge foundation. In Geotechnical Frontiers 2017 (pp. 657-666).

[33] Xiao, H., Qin, J., Ogai, H., & Jiang, X. (2015). A new standing‐wave testing system for bridge structure nondestructive damage detection using electromagnetic wave. IEEJ Transactions on Electrical and Electronic Engineering, 10(2), 157-165.

[34] Heymann, G., Rigby-Jones, J., & Milne, C. A. (2017). The application of continuous surface wave testing for settlement analysis with reference to a full-scale load test for a bridge at Pont Melin, Wales, UK. Journal of the South African Institution of Civil Engineering, 59(2), 49-58.

[35] Nguyen, T. D., Tran, K. T., & Gucunski, N. (2017). Detection of bridge-deck delamination using full ultrasonic waveform tomography. Journal of Infrastructure Systems, 23(2), 04016027.

[36] Chakraborty, J., Katunin, A., Klikowicz, P., & Salamak, M. (2019). Embedded ultrasonic transmission sensors and signal processing techniques for structural change detection in the Gliwice bridge. Procedia Structural Integrity, 17, 387-394.

[37] Sanderson, T., Freeseman, K., & Liu, Z. (2022). Concrete bridge deck overlay assessment using ultrasonic tomography. Case Studies in Construction Materials, 16, e00878.

[38] Erdogmus, E., Garcia, E., Amiri, A. S., & Schuller, M. (2020). A novel structural health monitoring method for reinforced concrete bridge decks using ultrasonic guided waves. Infrastructures, 5(6), 49.

[39] Cisem Altunayar Unsalan & Ozan Unsalan. (2024). Determination of the porosity of Didim H3-5 meteorite using pycnometry and three-dimensional laser scanning. Astrophysics and Space Science(12),119-119.

[40] Vladimir A. Prokhorov,Lev V. Kuzmin,Andrey A. Krivenko,Pavel A. Vladyka & Elena V. Efremova. (2024).

UWB Chaotic Pulse-Based Ranging: Time-of-Flight Approach. Technologies(12),269-269.

[41] Jun Wang,Zhen long Chen,Wei jie Yuan & Guang jun Shen. (2024). Hausdorff Measure of Space Anisotropic Gaussian Processes with Non-stationary Increments. Acta Mathematicae Applicatae Sinica, English Series(1),114-132.

[42] Žan Pleterski,Gašper Rak & Klemen Kregar. (2024). Determination of Chimney Non-Verticality from TLS Data Using RANSAC Method. Remote Sensing(23),4541-4541.